UNIVERSITÀ DEGLI STUDI DI PADOVA

Dipartimento di Fisica e Astronomia Galileo Galilei

Corso di Laurea in Fisica

Tesi di Laurea

A study of the ^{3}He+^{13}C reaction with the OSCAR apparatus

Studio della reazione ^{3}He+^{13}C con l'apparato OSCAR

Relatore
Dr. Tommaso Marchi

Corelatore
Prof. I. Lombardo
Prof. D. Dell'Aquila

Laureanda
Mualla Aytekin

Numero di Matricola
1225367

Academic Year
2021/2022

Abstract

The ^{13}C(^{3}He, $\alpha_{0,1,2}$)^{12}C reactions at sub-Coulomb energies present an opportunity to study the spectroscopy of the compound nucleus ^{16}O at relatively high excitation energies thanks to their high Q-value. ^{16}O is a self-conjugate nucleus meaning that a number of its excited states might be explained by the *quartet model*, which assumes the presence of quasi-single-particle structure of quartets, composed of 2 protons and 2 neutrons.

The experimental data available in the literature regarding these reactions is particularly scarse at low bombarding energies, where only old and incomplete data has been published, involving a limited range of angles and energies. With the HELICA experiment, the absolute cross sections of the ^{13}C(^{3}He, $\alpha_{0,1,2}$)^{12}C reactions were measured, for the first time, at 1.4 - 2.2 MeV bombarding energies over a large angular domain. The experiment exploited high-quality ^{3}He beams produced at the AN2000 accelerator of Legnaro National Laboratories (LNL), and a dedicated array of a new generation modular hodoscope: OSCAR.

This thesis introduces the theory behind the ^{13}C(^{3}He, $\alpha_{0,1,2}$)^{12}C reactions and deals with the detailed derivation of experimental absolute cross sections. The energy calibration of the silicon detectors of OSCAR is discussed with examples concerning various techniques that were used to calibrate different detection stages. The identification method is laid out for the reaction ejectile of interest, namely the α-particles. Lastly, new results of the absolute cross section and the angular distributions at various energies are presented and future studies are proposed to reveal possible resonance structures in the compound nucleus and the competition with direct processes.

Sommario

Le reazioni ^{13}C(^{3}He, $\alpha_{0,1,2}$)^{12}C a energie sub-coulombiane rappresentano una opportunità per studiare la spettroscopia del nucleo composto ^{16}O a energie di eccitazione relativamente alte grazie al loro alto Q-value. ^{16}O è un nucleo autoconiugato, nel quale un certo numero degli stati eccitati può essere spiegato dal *modello a quartetto*, che presuppone la presenza di una struttura quasi-particella-singola di quartetti composti da 2 protoni e 2 neutroni.

I dati sperimentali disponibili in letteratura su queste reazioni a basse energie di bombardamento sono vecchi e incompleti poiché coinvolgono un range limitato di angoli ed energie. Con l'esperimento HELICA, sono state misurate per la prima volta le sezioni d'urto assolute delle reazioni ^{13}C(^{3}He, $\alpha_{0,1,2}$)^{12}C a energie di bombardamento di 1.4 - 2.2 MeV. L'esperimento ha fatto uso dei fasci accelerati di ^{3}He prodotti dall'acceleratore AN2000 dei Laboratori Nazionali di Legnaro (LNL) e di un array dedicato di odoscopi modulare di nuova generazione: OSCAR.

Questa tesi introduce la teoria alla base delle reazioni ^{13}C(^{3}He, $\alpha_{0,1,2}$)^{12}C e si occupa della derivazione delle sezioni d'urto in unità assolute. La calibrazione in energia dei rivelatori al silicio di OSCAR è discussa con esempi riguardanti varie tecniche, che sono state utilizzate per calibrare i diversi stadi di rivelazione. Il metodo di identificazione utilizzato permette di misurare in modo non ambiguo leiettile di reazione di interesse, ovvero le particelle . Infine, vengono presentati i nuovi risultati della sezione d'urto in termini assoluti e delle distribuzioni angolari a varie energie, e vengono proposti possibili studi futuri per sondare strutture risonanti nel nucleo composto e il ruolo di effetti diretti.

Contents

1 Introduction

This thesis provides insights from the HELICA (Helion-Carbon scattering cross section for nuclear and applied physics) experiment which aims to measure, for the first time, the absolute cross section of ^{13}C(^{3} He, $\alpha_{0,1,2}$)^{12}C reactions at the AN2000 accelerator in INFN-LNL, at 1.4 - 2.2 MeV bombarding energies using a dedicated array of OSCAR telescopes. This experiment is particularly relevant because the experimental data previously published in the literature mainly consist of higher bombarding energies [1, 2, 3, 4] and a limited range of angles [5, 6, 7, 8]. The purpose of the experiment is to study the spectroscopy of the ^{16}O, which can be formed as the compound nucleus at very large excitation energies (above 22.8 MeV), to discover possible resonant states and to provide an insight into the reaction mechanism (*direct* vs. *compound nucleus*).

In this experiment, the excitation functions in absolute units can be obtained over an unprecedentedly large range of angles and impinging energies. These are of particular use also for Nuclear Reaction Analysis (NRA), since ^3He induced reactions at low energies can be exploited in ion beam analysis applications to surfaces of samples or thin layers. An example application of ^{13}C(^{3}He, $\alpha_{0,1,2}$)^{12}C reactions is the detection of ^{13}C traces and its ratio to ^{12}C inside materials containing light elements. Such a ratio can be used in a variety of fields, since, for example, it differs from its ordinary value in meteoric rocks [9], in athletes using steroids [10], and can be used as a biomarker in the detection of breast cancer cells [11].

1.1 (^{3}He, $\alpha_{0,1,2}$) reactions on ^{13}C

In nuclear physics, the energy of a reaction is determined by its Q-value, which corresponds to the difference in the binding energies between the final and the initial states of a reaction. The Q-value can be found also from the difference between the masses of reactants and those of the products. In the present case, the Q-value of the ^{13}C(^{3}He, α)^{12}C reaction involving ^{12}C at its

ground state, namely the ^{13}C(^{3}He, α_0)^{12}C reaction, is

$$Q = M(^{13}\mathrm{C}) + M(^{3}\mathrm{He}) - M(^{12}\mathrm{C}) - M(^{4}\mathrm{He}) = 15.631\,MeV$$

where the masses are measured in MeV/c^2, and can be extracted, for example, from Refs. [12, 13]. When a particle is left at its excited state at an excitation energy E_x, the Q-value becomes $Q' = Q - E_x$. Therefore, the Q-values of the ^{13}C(^{3}He, $\alpha_{1,2}$)^{12}C* reactions, leaving the residual ^{12}C*, respectively, in its first ($E_{x,1}$ = 4.44 MeV) and second ($E_{x,2}$ = 7.65 MeV) excited states, are:

$$Q_1 = Q - E_{x,1} = 11.191MeV \quad Q_2 = Q - E_{x,2} = 7.977MeV$$

In all of these cases, $Q > 0$ meaning that the reaction is *exoenergetic* and it can take place with relatively slow incident particles as opposed to an *endoenergetic* reaction, where the particles should meet a threshold energy for the reaction to occur.

The initial state, which is the same for all the three reactions, ^{3}He + ^{13}C, has a total binding energy of 104.826 MeV. After the collision of these two nuclei, we might obtain an excited compound nucleus of ^{16}O in the intermediate state, that has a binding energy of 127.619 MeV in its *ground state*. Consequently, depending on the energy of the ^{3}He projectile we might populate the compound ^{16}O nucleus at high excitation energies $E_x > 24$ MeV. When the reaction proceeds through intermediates states of ^{16}O, then it is called a *compound nucleus* reaction, and it is influenced by the spectroscopy of the populated states. More *direct* reaction mechanisms that lead to the same reaction products, such as a neutron pick-up, are less likely to occur, since the reaction is investigated in this work at considerably low energies (1.4 - 2.2 MeV), well below the Coulomb barrier ($U \approx 3.8MeV$).

The first of the three reactions mentioned above, ^{13}C(^{3}He, α_0)^{12}C, has a final state of ^{12}C + α with carbon at its ground state which is a 0^+ state. The sum of the binding energies of these two particles is 120.457 MeV which is lower than that of the initial state. In the second reaction, ^{13}C(^{3}He, α_1), the ^{12}C is at its first excited state at 4.44 MeV which is a 2^+. The third reaction, ^{13}C(^{3}He, α_2)^{12}C*, results in a ^{12}C at its Hoyle state that is a 0^+ at 7.65 MeV.

The angular distributions, at a certain energy, of the emitted α particles are connected to the angular momentum transferred to it. Taking into account angular momentum transferred to α, which is reflected in the angular distribution of the differential cross-section and the J^π of the residual nucleus, it is possible to deduce the spectroscopic properties (J^π) of the compound nucleus formed the intermediate state, thus obtaining information about the spin and angular momentum of the excited ^{16}O corresponding to the resonance.

Other than the (^{3}He, α_0) reaction, the collision might result also in elastic scattering as well as inelastic scattering if the final state consists of an excited ^{13}C. In both cases, the energy of the ^{3}He is considerably lower than that of

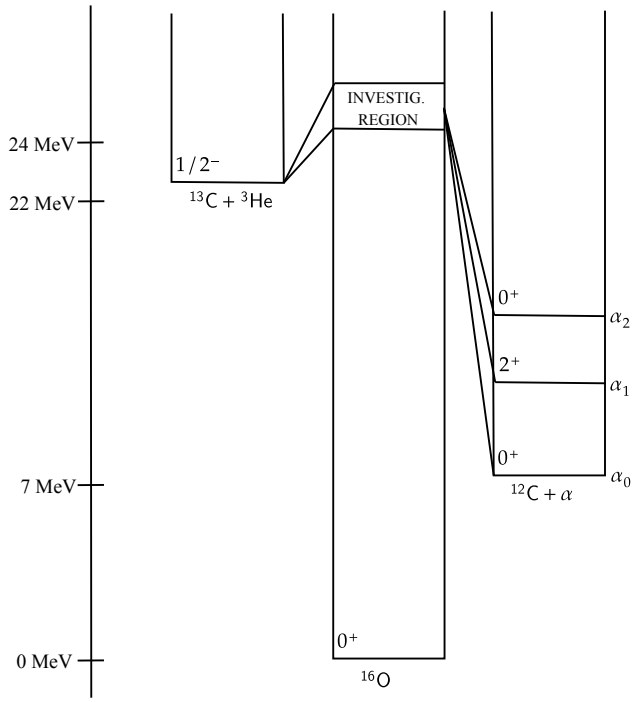

Figure 1.1: Diagram illustrating the energy levels of initial, intermediate and final states in the ^{13}C(^{3}He, $\alpha_{0,1,2}$)^{12}C reactions.

the α particles from the reactions of interest, due to the exothermic nature of the ^{13}C(^{3}He, $\alpha_{0,1,2}$)^{12}C reactions. To avoid contamination from elastic scattering events, which have a particularly high rate at these energies, all the detectors in the apparatus were preceded by a calibrated Mylar absorber, which stops the elastic ^{3}He nuclei, while the ejectiles of interest are only slightly degraded in energy.

Furthermore, ^{12}C + $\alpha_{0,1,2}$ exit channels are not the only final states available at energies from 1.4 to 2.2 MeV. An overall list of reaction products is presented in Table 1.1.

1.2 Previous Measurements

Concerning the ^{13}C(^{3}He, $\alpha_{0,1,2}$)^{12}C reactions, data present in the literature belong mainly to high energies, where more direct reaction mechanisms are typically favoured as opposed to the formation of a compound nucleus [1, 2, 3, 4]. Kellogg and Zurmuhle studied the reaction at 12, 15 and 18 MeV. As in the case of all other articles concerning high energy, they propose a direct pick-up mechanism and proceed into calculating optical parameters with distorted-wave Born approximation. Nevertheless, Deshpande confirms that, due to the configuration of ^{12}C in the Hoyle state, the $\frac{1}{2}^{-}$ -> 0^{+} transition requires a compound

Reaction Products	Q-Value (keV)		Threshold (keV)	
$^{16}O + \gamma$	22793.2304	4	0	
$^{12}C + \alpha$	15631.3		0	
$^{15}N + p$	10665.8191	6	0	
$4\,\alpha$	8356.5647	4	0	
$^{8}Be + 2\,\alpha$	8264.72	4	0	
$^{15}O + 2\,n$	7129.3	5	0	
$^{14}N + d$	2057.0885	3	0	
$^{14}C + 2\,p$	458.393	4	0	
$^{13}C + {}^{3}He$	0		0	
$^{13}C + p + d$	0		0	
$^{13}C + 2\,n + 2\,p$	0		0	
$^{14}N + 2\,n + p$	-167.4777	6	205.9273	7
$^{11}B + p + \alpha$	-325.367	12	400.065	15

Table 1.1: The possible reaction products of $^{3}He + {}^{13}C$ at $1.4 \leq E_{beam} \leq 2.2$MeV extracted from Q-value calculator of NNDC database at Ref. [14]

nucleus formation and cannot be explained by a simple pick-up process. Both Gulamov et al. and Nassurlla et al. highlight the significance of the high Q-value of the $(^{3}He, \alpha)$ reaction as opposed to those of (p, d) or (d, t) reactions, and its contribution to the momentum mismatch between the reactants and the products suggests the involvement of more complicated reaction mechanisms.

As far as bombarding energies at the range of HELICA experiment are concerned, Holmgren provides with the differential cross section measurements, yet with relatively low accuracy (25%) and, unfortunately, at only one bombarding energy, 2.00 MeV [5]. The authors compare these results with those at a bombarding energy of 4.50 MeV, even if the angular distributions for the second set of data are in relative units and the absolute cross section is not measured [6]. In a paper from the late '60s, Weller claims that the influence of the ^{16}O structure is essential to study the ^{3}He induced reaction on ^{13}C from 2.00 to 8.00 MeV. In Ref. [7], they compare excitation functions of $^{13}C(^{3}He, \alpha_0)^{12}C$ as well as $^{13}C(^{3}He, {}^{3}He)^{13}C$ and $^{13}C(^{3}He, p)^{15}N$ to inspect a resonance structure at 6.0 MeV bombarding energy. The most recent data is from a 1989 article, where the $^{13}C(^{3}He, \alpha_0)^{12}C$ reaction is studied at $E_{cm} = 1.20$ and 1.05 MeV. In this case, the authors make the assumption of a direct reaction where two mechanisms compete: a heavy-particle stripping (Be-9) and a neutron pick-up [8].

1.3 The Spectroscopy of ^{16}O

In nuclear physics, there are many models aiming to describe the structure of the atomic nucleus. One of these is the *nuclear shell model*, which is a gen-

eralization of *Fermi gas model* and is very similar to how electrons arrange in an atom. *Nuclear shell model* is a quantum model where single particles interact with a mean nuclear field and fill energy levels determined by the solution to the Schrödinger's equation. When combined with Woods-Saxon potential and considerations relating to Spin-Orbit interaction are taken into account, the model explains why nuclei having certain "magic" number of neutrons or protons appear to be particularly stable. The ^{16}O is a nucleus that is doubly-magic since it has 8 neutrons and 8 protons. Given that it is an even-even nucleus, its ground state has a spin-parity of 0^+.

Another model capable to describe systematic properties of the atomic nucleus is the *liquid drop model*, which is a collective model that draws an analogy between the inter-molecular forces in a liquid drop with that of the nuclear force. This model, along with describing the trend of binding energies of nuclei having the same mass, A, foresees vibrations in the surface and possible deformations leading to excited states in nuclei. An example of quadruple vibration can be seen in the energy level diagram of ^{16}O in Figure 1.2, where states of spin-parity $2^+, 4^+, 6^+ \ldots$ appear to be equally distanced ($\Delta E = \hbar\omega_2 =\sim 6.9 MeV$) since the vibrational modes are harmonic oscillators of frequency ω_2. Other levels present in the diagram can be studied with this model, though it is not within the scope of this thesis.

An important characteristic of ^{16}O nucleus is that it is self-conjugate, meaning that it is an even-even nucleus with $N = Z$. Self-conjugate nuclei are known to excite states up to 30-40 MeV and have an α-separation threshold lower than that of a nucleon separation [16]. Studying the energy levels of ^{16}O, one can observe that the proton separation energy (S_p) is 12.1 MeV and neutron separation energy (S_n) is 15.6 MeV, which are both well larger than the separation energy of an alpha particle (S_α = 7.2 MeV). This behavior is explained by Arima, Gillet, and Ginocchio by the presence of quasi-single-particles of quartets (containing 2 protons and 2 neutrons). Similarly, ^{12}C in the final product of the reaction is another self-conjugate nucleus prior to ^{16}O, meaning that it differs only by an α particle, which already exists as a quartet in ^{16}O. This description of the atomic nucleus, which is known as *quartet model* [16], allows to describe, in a systematic way, the energy of a number of excited states of even-even nuclei, from ^{12}C up to ^{52}Fe. Experimentally probing the spectroscopy of ^{16}O at high excitation energies, where the quartet model predicts quartet excitations, is crucial to test the prescriptions of the quartet model and contribute to understanding the complex proton-neutron correlations in the atomic nucleus and the dynamics of proton-neutron systems.

1.4 Nuclear Reaction Kinematics

The energy available for the system while forming a compound nucleus is that of the center-of-mass reference frame as opposed to that of the *laboratory*

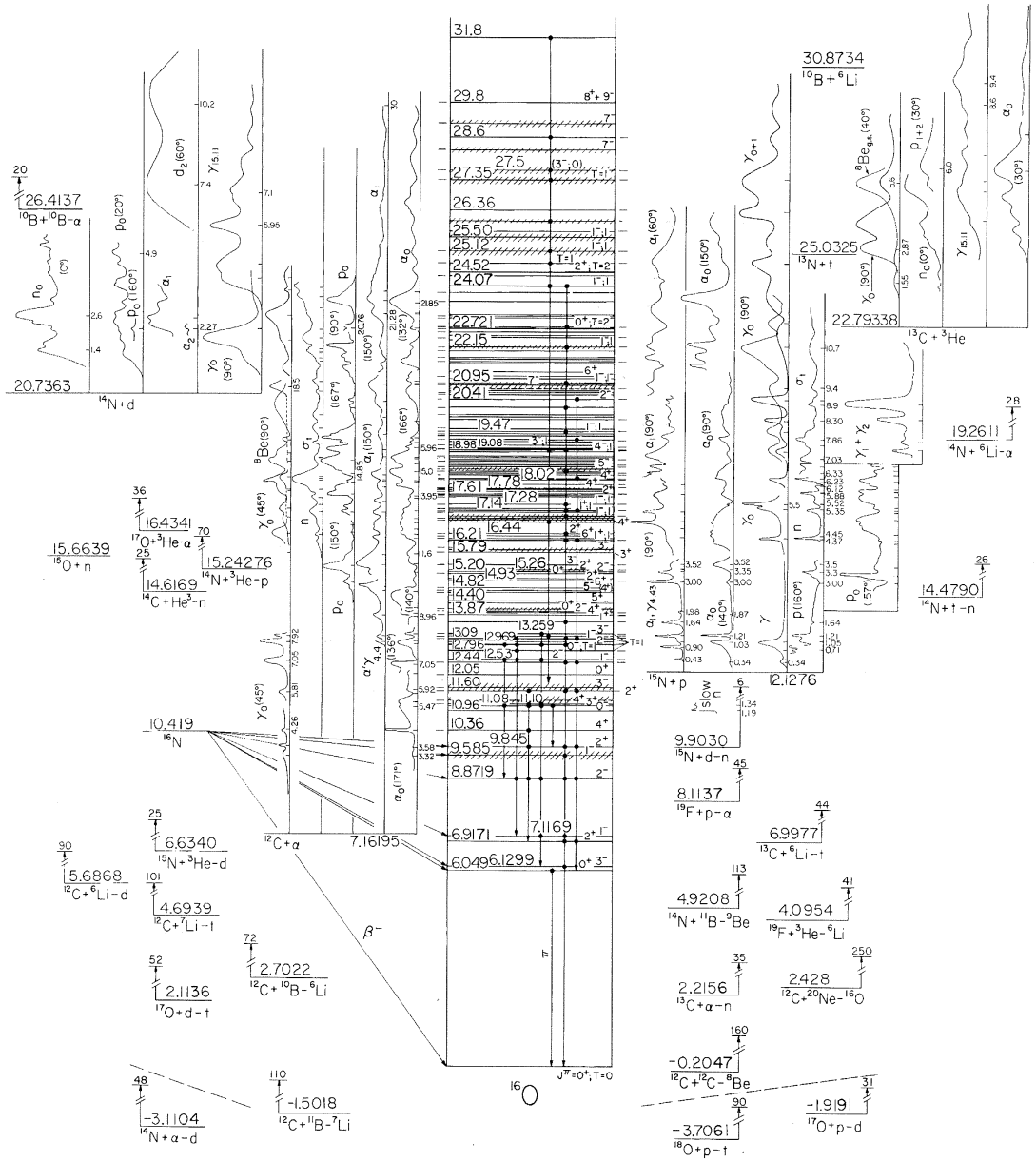

Figure 1.2: Energy level diagram of ^{16}O extracted from Ref. [15]. The energy levels of the possible decay products with respect to the ground state of ^{16}O are illustrated at the sides along with the excitation functions belonging to: (^{14}N + d) (^{12}C + α) (^{15}N + p) and (^{13}C + ^{3}He).

frame. In a generic nuclear reaction A(a,b)B at low impinging energy, one can neglect the relativity and, using momentum conservation, the velocity of the center of mass of the collision partners can be expressed as:

$$v_{CM} = \frac{m_a}{m_a + m_A} v_a$$

Consequently, the energy available for the compound nucleus formation, i.e. the kinetic energy in the center-of-mass-frame, is:

$$E_{CM} = E_{beam} - E_{k,CM} = \frac{1}{2} m_a v_a^2 + \frac{1}{2} (m_a + m_A) v_{CM}^2 = E_{beam} \frac{m_A}{m_a + m_A}$$

where E_{beam} is the beam energy, which is given in the laboratory frame of reference. It is clear that the energy available in the center-of-mass is always lower than that in the laboratory frame, due to the motion of the center of mass.

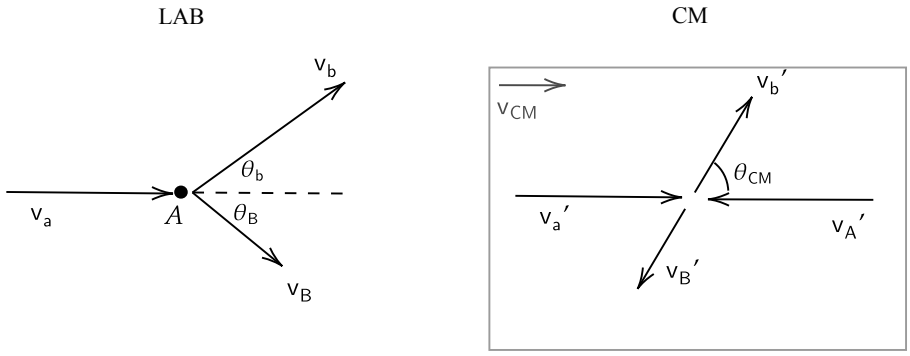

Figure 1.3: Diagram illustrating kinematics of a two body collision in the laboratory and center of mass frames

Another important consequence of the reaction kinematics is that the energy of the ejected particle b depends on the polar angle at which it is emitted. To find this energy, we can use the conservation of energy and the conservation of momentum in two directions: parallel and perpendicular to the beamline as can be seen in Figure 1.3. From these three conservation laws, we obtain three equations with 2 unknown variables v_b and v_B.

$$\begin{cases} Q + \frac{1}{2} m_a v_a^2 = \frac{1}{2} m_b v_b^2 + \frac{1}{2} m_B v_B^2 \\ m_a v_a = m_b v_b \cos(\theta_b) + m_B v_B \cos(\theta_B) \\ 0 = m_b v_b \sin(\theta_b) + m_B v_B \sin(\theta_B) \end{cases}$$

Resolving this system of equations, one obtains the energy of the ejected particle b as a function of the angle (both in the laboratory frame of reference):

$$\sqrt{E_b} = \frac{\sqrt{m_a\, m_A\, E_{beam}}\cos(\theta_b)}{m_b + m_B} + \sqrt{\left(\frac{\sqrt{m_a\, m_A\, E_{beam}}\cos(\theta_b)}{m_b + m_B}\right)^2 + \frac{m_B\, Q + (m_B - m_b)E_{beam}}{m_b + m_B}} \tag{1.1}$$

From this equation, we can calculate the energy at which α particles will be emitted in different directions which respect to the direction of the beam exploiting the Q-value of the reaction and the beam energy.

Once the energy, or the velocity, of the ejected particle b is known, we can transform the laboratory angle to that of the center-of-mass considering that the velocity parallel to the beamline in the laboratory frame is the parallel velocity in the center-of-mass frame plus the velocity of the center-of-mass, whereas the perpendicular velocities are the same.

$$\begin{cases} v_b\, \cos(\theta_b) = v'_b\, \cos(\theta_{CM}) + v_{CM} \\ v_b\, \sin(\theta_b) = v'_b\, \sin(\theta_{CM}) \end{cases}$$

Thus, we can compute the angle of the ejected particle in the center of mass as

$$\tan(\theta_{CM}) = \tan(\theta_b) - \frac{v_{CM}/v_b}{\sin(\theta_b)}$$

2

Experimental Setup and Detector Calibration

The experiment was performed at the AN2000 van de Graaf accelerator of the INFN - Laboratori Nazionali di Legnaro (Padua, Italy). A $^{3}He^{+}$ beam is produced by the internal ion source at an intensity range of 70 to 190 nA depending on the energy of the beam. Two sets of runs are carried out during the summer of 2021 in July and September.

2.1 Target Characteristics

The targets used in this experiment were produced by the *Laboratorio Bersagli* of INFN - Laboratori del Sud (Catania, Italy). The main target used during the experiment is made of ^{13}C and has a thickness of ($29 \mu g/cm^2$). Other targets (thick), containing a mixture of carbon isotopes with different, calibrated, conentrations of ^{13}C (5, 15, 25 and 45%) were also used to carry out examplary NRA measurements. A set of measurements are finally taken with ^{11}B and LiF targets as reference for future experiments.

2.2 The detection system

OSCAR (hOdoscope of Silicons for Correlations and Analysis of Reactions), is a new generation modular hodoscope, based on two segmented detection stages (20 μm Single Sided Silicon Strip Detector (SSSSD) - 500 μm Silicon pads). It is characterized by a good energy resolution and high versatility for its compactness. The SSSSD is made of a thin silicon wafer, whose electric contact on the front surface is segmented into 16 aluminum vertical strips having a width of 3.125 mm, and an inter-strip of about 0.125 mm. 16 electric lines leave the silicon surface through a ceramic frame and connect to a charge-sensitive pre-amplifier

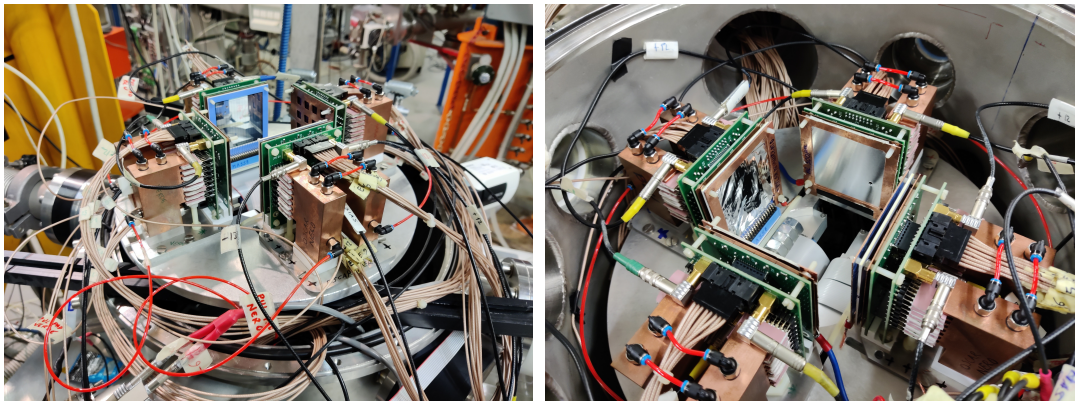

(a) **(b)**

Figure 2.1: Photographs of the detection system taken on 18/07/2021 (a) and 21/07/2021 (b). (a) 4 OSCAR telescopes during preparation on the metal plate. The strips of *OSCAR Nero* and pads of *OSCAR Rosso* can be seen in the background. (b) The detection system, placed in the reaction chamber after the Mylar foils, and aluminum absorbers are assembled in front of the telescopes. The cables connecting the pre-amplifiers to the amplifiers outside the reaction chamber are featured in both (a) and (b).

that is placed within the vacuum chamber with the hodoscope to reduce noise. The silicon is polarized to a bias of 3.0 V. The second detection stage is made of 16 silicon pads on a ceramic support, each with an active area of 1 cm^2. The pads are welded to a printed circuit board which is connected to a second board containing the pre-amplifiers.

During the experiment, an array of 4 OSCAR telescopes is used. *OSCAR Blu* and *OSCAR Verde* were positioned after the target with respect to the incoming beam, to cover forward angles, while *OSCAR Nero* and *OSCAR Rosso* were positioned before the target to cover the backward angles, as can be seen from Figure. 2.2. Two of the telescopes (*OSCAR Verde* and *OSCAR Rosso*) have only one stage consisting of 16 silicon pads. As mentioned before, to minimize the dead-time due to the elastic-scattering of helium-3, since scattering occurs at a higher rate compared to reactions, absorbers were positioned at the entrance windows of the telescopes. They consisted of thin Mylar foils (6.0-9.5 μm) for two OSCAR modules with the SSSSD, and of thicker aluminum foils (500-600 μm) for the pads. Nevertheless, one of the pads of *OSCAR Rosso*, at the most backward angle, was dedicated to measuring the occurrence of elastic scattering. To this end, a hole was created in the aluminum absorber preceding its position. This detector, from now on, will be called the *elastic monitor*, as it is used to monitor the rate of elastically scattered ^{3}He during the experiment.

The geometry of *OSCAR* is determined by the possible intersections of the 16 strips with 16 pads, which make a total of 64 combinations (see Figure 2.2) that from now on will be called *pseudo-telescope*. The number of events that reach a point on the hodoscope depends on the polar angle with respect to the beam

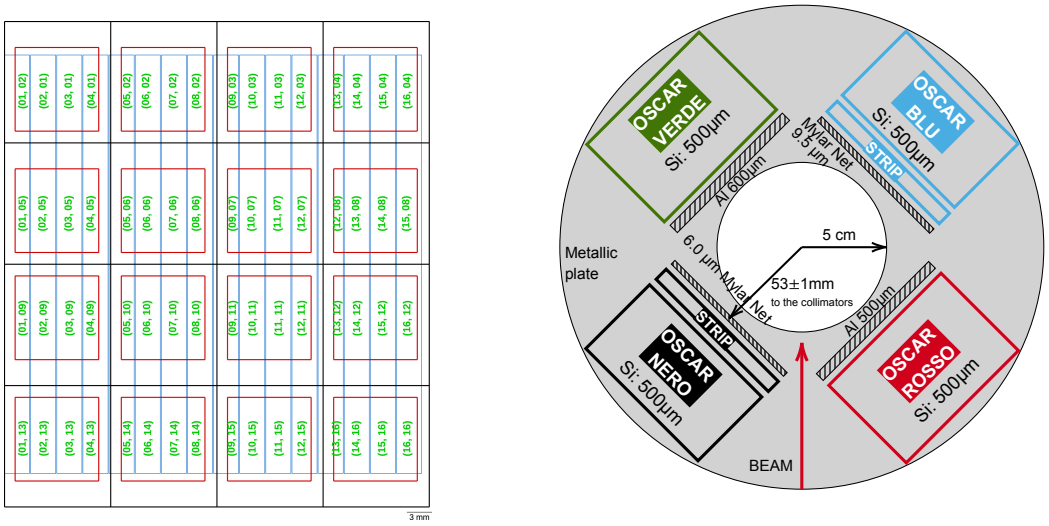

(a) **(b)**

Figure 2.2: OSCAR geometry. (a) A schematic view of a two layer OSCAR telescope's layout where each pseudo-detector is indicated as (pad,strip) combination [17]. (b) A diagram featuring the 4 OSCAR telescopes and how they are positioned in the reaction chamber with respect to the beam line.

line. Since detectors have a finite area, during characterization of the apparatus in Ref. [17], a Monte-Carlo simulation was carried out to assign average angles to the single detectors (strips or pads) as well as to the pseudo-detectors. Similarly, the larger the solid angle covered by a pseudo detection unit, the higher will be the number of events detected by it. Thus, the solid angle covered by each pseudo-telescope on the array is estimated by the simulation. The bordering strips (first and last) that are aligned with a pad have a region that overlap the ceramic support instead of the pad. This geometrical mismatch results in the reduction of the active are of the pseudo-telescopes. To account for this effect, we will consider only the central two pseudo-detectors for each pad for the experimental results.

Another important point to take into account is the dis-uniformity in the first detection layer, due to the difficulty of manufacturing thin silicon wafers. The detector thickness is measured to have a maximum variation from 11.5 μm to 25.6 μm [17]. The thickness seems to have slightly different average values between the two first stages of the two OSCAR telescopes, *Blu* having a higher average value. The consequence of such a variation is discussed later during the calibration procedure.

2.3 Data Acquisition and Processing

The output signals from the pre-amplifiers are collected and delivered to the amplifiers with integrated logic circuits for generating trigger signals. The logic

or of all such signals from all the silicon pads in the array, is used to produce a gate for the "FAIR" data acquisition system. The files generated by the DAQ FAIR for a given run identified by the time of acquisition are unpacked into a raw data file easy to read for successive analysis. The raw data is then mapped into specific detector data structures and eventually energy-calibrated once the calibration parameters of each detection unit are obtained. There are two further processes that are necessary to have data ready for analysis: identification, which determines the A and Z of the particle detected in an event, and pixelization, which eliminates the events deriving from signals from the adjacent strips to the strip that the particle interacted with and produces meaningful particle tracks in the detectors. The latter procedure is trivial for the two OSCAR modules that do not have the first detection stage.

2.4 Detector Calibration

The calibrations of detectors are based on dedicated calibration runs that were carried out during the first day of the accelerator beam in July 2021. These runs consist of:

- Three-peaked α source (directed towards each hodoscope)
- Elastic scattering of protons on Au (150 $\mu g/cm^2$) at the following energies: 0.7, 0.8, 1.7, 1.8, 1.9, 2.0 MeV
- Elastic scattering of protons on C-12 (15 $\mu g/cm^2$) at the following energies: 0.9, 1.0, 1.1, 1.2, 1.3, 1.4, 1.9, 1.95, 2.0, 2.05 MeV

While for the calibration of the pads of *OSCAR Rosso* and *OSCAR Verde* and of the strips of *OSCAR Blu* and *Nero* these runs were sufficient, for the calibration of the second stage of detectors, meaning the pads of *OSCAR Blu* and *OSCAR Nero*, an experimental run at 1.804 MeV is used, exploiting well-identified $^{13}C(^{3}He, \alpha_{0,1,2})^{12}C$ reactions.

There has been also an adjustment of gains during the experiment when it has been noticed that the electronic configuration of the second stage pads were insufficient for detecting certain low energy particles, it was decided to increase the gains of the amplifiers. Furthermore, a similar set of calibration runs are carried out for the second set of runs in September 2021 and their results are compared to the ones obtained previously though they are not reported in this thesis.

2.5 Calibration procedure for the first stage

The first step towards calibrating the first stage detectors has been creating the histograms from the mapped raw data for each of the 32 pads (of OSCAR telescopes having single stage) and 32 strips (of OSCAR telescopes having two stages).

Calibration with Alpha Source

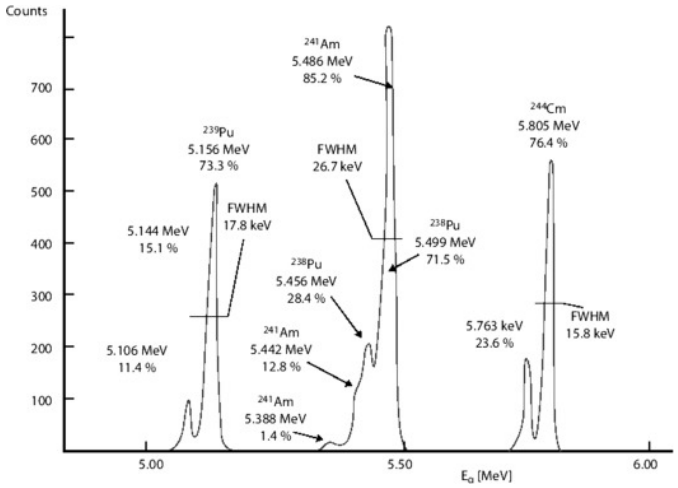

Figure 2.3: An example spectrum of an alpha source from Ref. [18].

The first calibration technique that will be discussed is the use of the spectrum of an α-source. The α-source used during this experiment has three peaks that are due to Pu-239, Am-241 and Cm-244, from left to right as can be seen in Figure 2.3.

Thanks to the high resolution of the detectors, it was possible to identify the secondary peaks in the histograms provided by the calibration runs, see Figure 2.4a. The bin range for the fits is determined manually by visualizing the relevant histograms and by zooming in the regions where the peaks appear. During such procedure, the bin at which the two Gaussian distributions overlap is also identified to be provided to the fit as an additional parameter. Based on the resolution of each individual detection unit, 1 to 3 peak centers and their errors are recorded along with the corresponding known energies for each of the three sources.

The simple procedure discussed above is used for the pads of *OSCAR Rosso* and *OSCAR Verde* and the strips of *OSCAR Nero*, since α-particles are not stopped fully in the case of *OSCAR Blu*. After the initial calibration using the α-source is done, the two-dimensional histograms of α-spectra are plotted to cross-check if the calibration applies correctly over various detectors, see Figure 2.5. For each detector number, the α-spectra present peaks at the same positions after their calibrations though the width of the peaks differs due to small differences in the quality of the silicon detectors and the electronic chains. The measurements provided by the strips show greater noise than that of the pads. Furthermore, the resolutions of certain *OSCAR Verde* pads are much lower than the rest due to the damage caused by a black-out during the experiment.

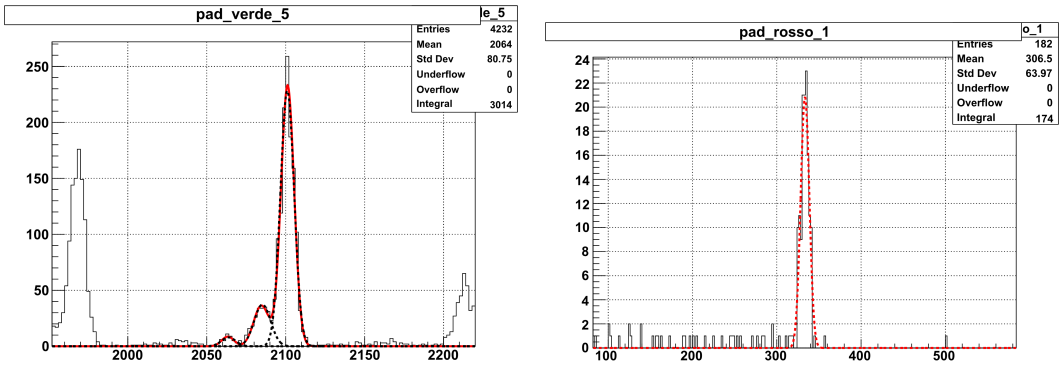

(a) Example multi-Gaussian fit of an alpha peak belonging to the Am source.

(b) Example fit for elastic scattering of protons on gold at 0.8 MeV

Figure 2.4: Extraction of calibration points from not one-dimensional histograms

Calibration with Elastic Scattering of Protons on Gold and on Carbon-12

To add additional calibration points, and further improve the calibrations, it was also considered the elastic scattering of protons of various energies on two different targets: a gold target of 150 $\mu g/cm^2$ and a carbon target of 15 $\mu g/cm^2$. Unlike α-source, which emits α-particles at a given energy, the energy of the protons after the scattering depends on the angle. Using the previously derived formula in Section 1.4, (1.1), the energy of the scattered particle, for example on gold, with a negligible target thickness can be computed as:

$$\sqrt{E(\theta)} = \frac{\sqrt{m_p\, m_{Au}\, E}cos(\theta)}{m_p + m_Au} + \sqrt{(\frac{\sqrt{m_p\, m_{Au}\, E}cos(\theta)}{m_p + m_{Au}})^2 + \frac{(m_{Au} - m_p)E}{m_p + m_{Au}}}$$

Nevertheless, the target has a finite thickness, and protons, being charged heavy particles, deposit energy while passing through the target. To correctly compute these effects, it was assumed, for simplicity, that the elastic scattering takes place at the middle of the target, on average. With this assumption, we calculated the energy with which the protons arrive at a specific detector for a given beam energy considering the following three quantities:

1. Energy loss of the incident beam for having crossed half of the thickness of the target.
2. Energy of the elastically scattered proton according to the reaction kinematics and depending on the angle corresponding to the detector in question.
3. Energy loss of the outgoing elastically scattered proton for crossing the target depending on the angle since the path that the particle will cross is given by half of the thickness divided by the cosine of the angle.

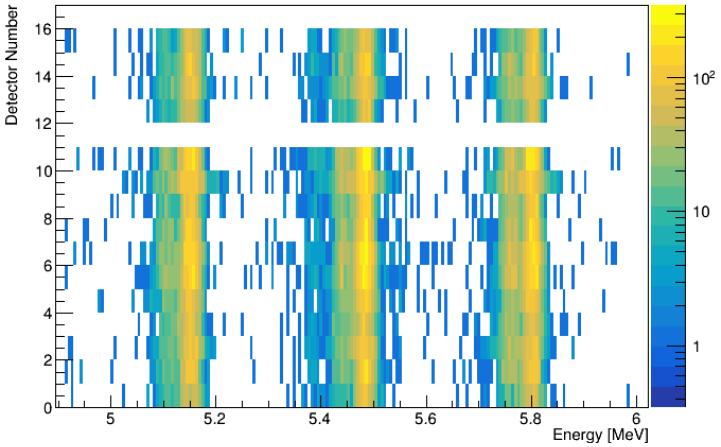

(a) Detector number vs energy for all pads of *OSCAR Rosso*

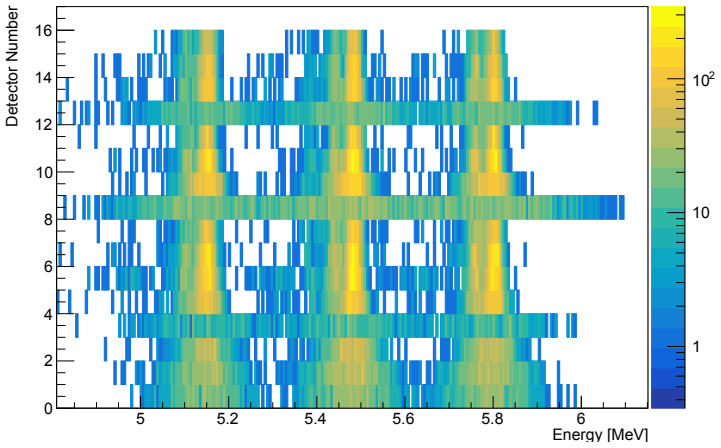

(b) Detector number vs energy for all pads of *OSCAR Verde*

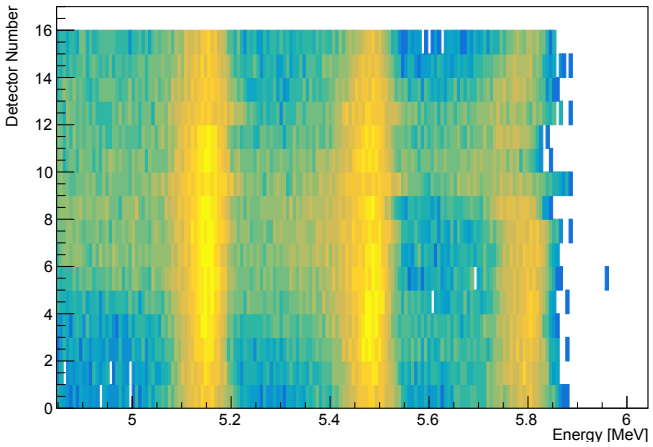

(c) Detector number vs energy for all strips of *OSCAR Nero*

Figure 2.5: Two-dimensional histograms featuring detector number versus energy. The position of the elastic monitor is empty since it is calibrated separately.

Such calculations are carried out using stopping power data extracted from *LISE++* software [19], and the data by Huang et al. and Wang et al. for nuclear masses [12, 13]. To associate the remaining energies to the ADC values, the peaks found in the histograms are fitted with a Gaussian distribution. To do so, the range of the histogram (which is from 0 to 4096) is limited to a certain range to discard the possible presence of the pulser signals, which was also used for dead time monitoring during all the experiment, and the exponentially increasing noise that appears for the low ADC values. An example histogram is shown in Figure 2.4b, alongside with a typical Gaussian fit.

The figures saved are then carefully checked to ensure that the fits are performed correctly and the cases where it was necessary to discard the information obtained from a certain fit, especially in the case of strips, for various reasons that include the inability to identify the peak due to high noise, the presence of a double peak and missing polarization in the case of the strips of *OSCAR Blu* for certain runs, see Figure 2.6.

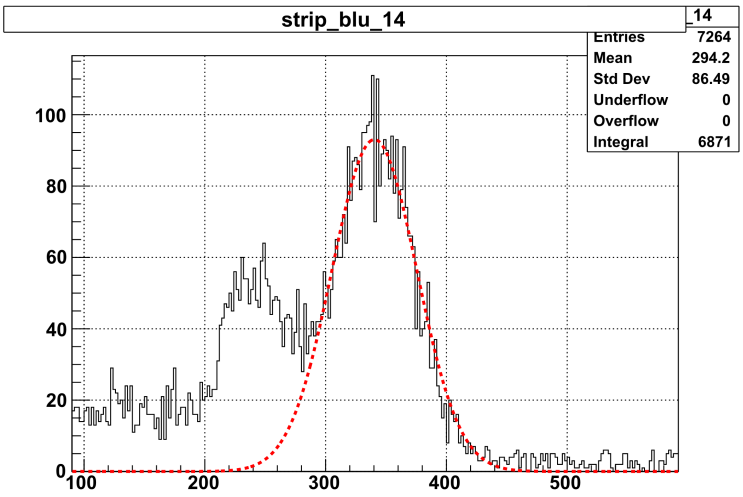

Figure 2.6: Example case for a discarded fit where there is a secondary peak formation.

After having recorded the data points with means from the fits in ADC values and the corresponding energies in MeV for each detector, a linear fit ($E = m_b\, ADC + q$) is performed as shown in Figure 2.7. The fits are more than satisfactory as the corresponding energy constraints cover a wide range of energies thanks to the simultaneous use of α-particles and elastic scattering data of protons.

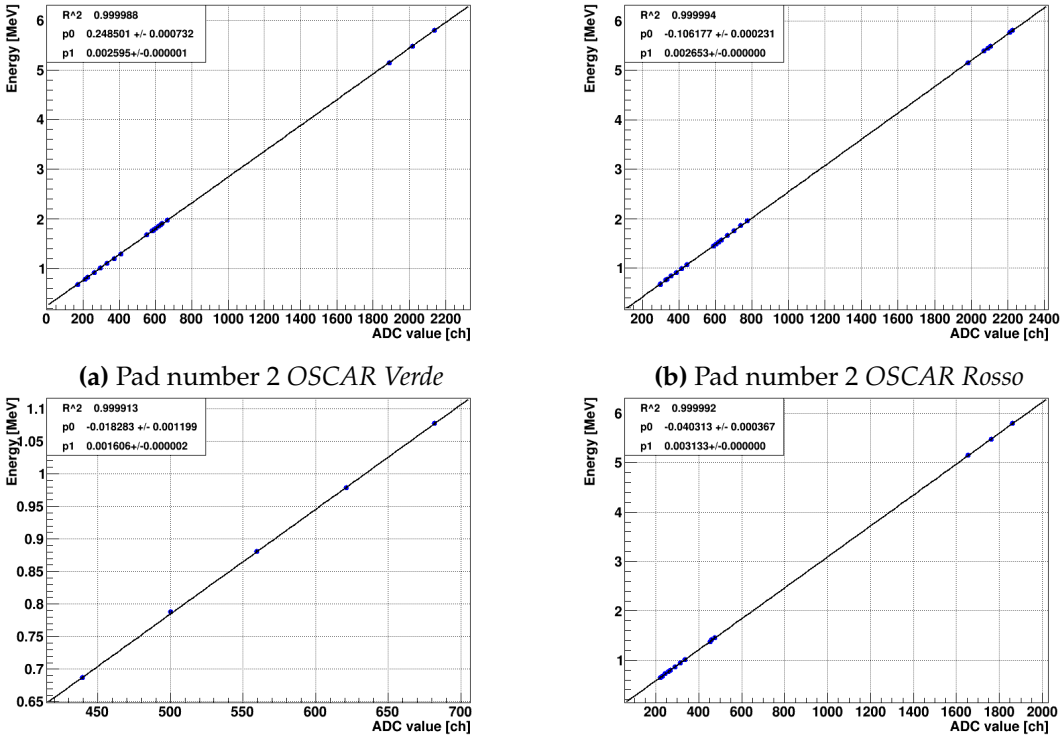

(a) Pad number 2 *OSCAR Verde*

(b) Pad number 2 *OSCAR Rosso*

(c) Strip number 2 *OSCAR Blu*

(d) Strip number 2 *OSCAR Nero*

Figure 2.7: Example linear fits carried out to obtain calibration coefficients.

2.6 Calibration procedure for the second stage

Calibration with Alpha Source

When α-particles emitted from the calibration source are in transmission, i.e. they are detected from both first and second detection stages, which is the case only for *OSCAR Blu* since the strips of *OSCAR Nero* are slightly thicker, the calibration of the second stage is done through the use of a $\Delta E - E$ with calibrated ΔE and non-calibrated E. To do so, the regions of the three different alpha emissions were identified from the $\Delta E - E$ plots generated for 16 pads, each of which contains the sum of the events coming from the 4 pseudo-detectors, see Figure 2.8. From these plots, for each event, a point for the linear regression is generated by subtracting the energy deposited in first layer from the α-particle energy in MeV and associating it to the value read in the x-coordinate for the second layer.

Calibration with $^{13}C(^3He, \alpha_{0,1,2})^{12}C$ reaction

Since the use of alpha particles was not applicable for the pads of *OSCAR Nero* (as well as scattered protons which are at lower energy) due to the thickness of the strips, we have decided to use experimental data from nuclear reactions

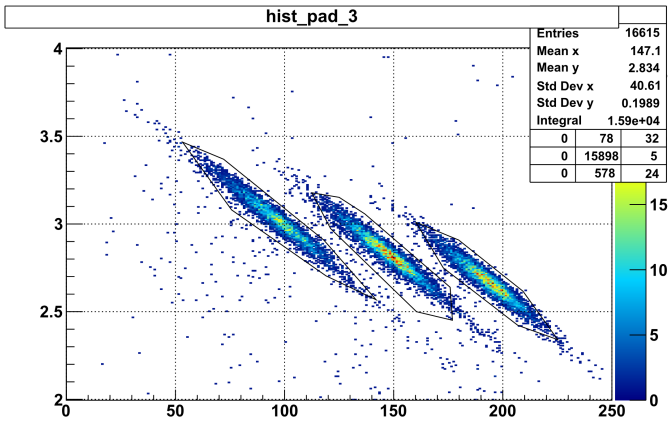

Figure 2.8: Examples cuts for determining events from a ΔE plot (y-axis in MeV and x-axis in ADC channels) of *OSCAR Blu*

induced by ^{3}He beams. As done for the α-source data, each event constitutes a given calibration point in the bi-dimensional plot. Firstly, for *OSCAR Nero* pads, two regions for ^{13}C(^{3}He, $\alpha_{0,1}$)^{12}C reactions were identified from the $\Delta E - E$ plots. ^{13}C(^{3}He, α_{2})^{12}C was excluded since it does not appear for all angles at these energies. While in the case of *OSCAR Blu* it was possible to use α-particles, we have chosen to improve the quality of their calibration by increasing data points adding the events regarding α_0. For each event, the energy of the particle reaching the first layer of detection is calculated as $\Delta E + E$. The areas chosen from ΔE-E plots are shown in Figure 2.9.

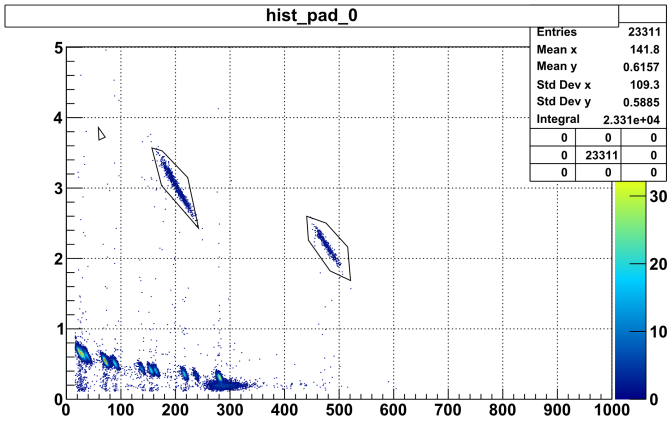

Figure 2.9: Examples cuts for determining events from a $\Delta E - E$ plot of *OSCAR Nero*

At a given beam energy, the energy of the ejected particle for the particular ^{13}C(^{3}He, $\alpha_{0,1,2}$)^{12}C reaction can be calculated according to Equation 1.1. The same calculations concerning the energy loss due to target thickness are carried out for the carbon-13 target used during the experiment. In other words, for

each event, given the angle corresponding to each pseudo-detector the following points are taken into account:

- Energy loss of the incident beam for having crossed half of the thickness of the target.
- Energy after the interaction given by $^{13}C(^{3}He, \alpha_{0,1,2})^{12}C$.
- Energy loss of the ejected particle for crossing a path within the target.
- Energy loss of the ejected particle crossing the Mylar foil preceding the SSSSDs.
- Energy deposited in the first stage (from the y-coordinate of the ΔE-E plot).

The linear fit points for the calibration are therefore extracted from the ΔE-E plots by associating the calculated energy deposited in the second stage to the energy corresponding to the ADC value in the x-coordinate. Using the data points obtained from the α-source and experimental data, the linear regression for the calibration of the second stage detection is performed as shown in Figure 2.10.

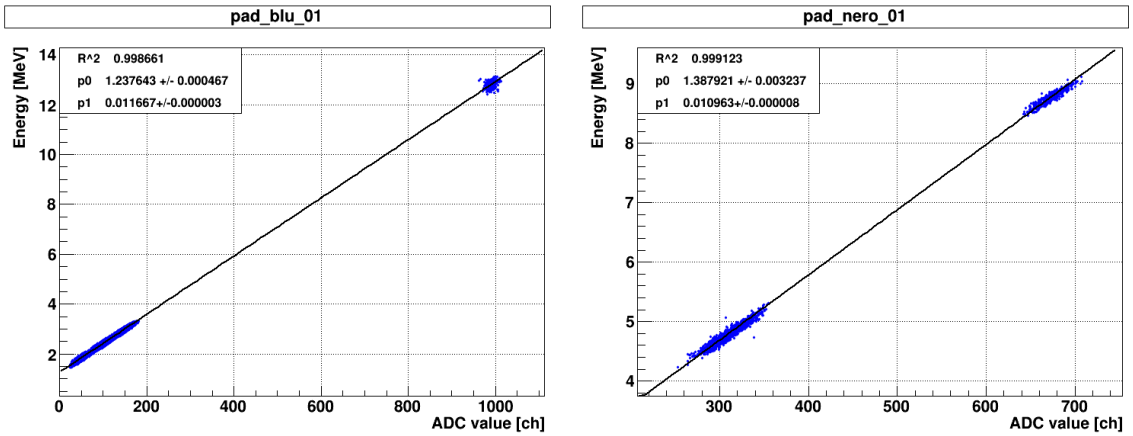

(a) Pad number 1 *OSCAR Blu*

(b) Pad number 1 *OSCAR Nero*

Figure 2.10: Example linear fits carried out to obtain calibration coefficients of the second stage detectors

2.7 Gain Adjustments

During the experiment, it was noted that the amplification of the pads of *OSCAR Blu* and *OSCAR Nero* were not sufficient to make full use of the input voltage range, thus required an increase. The adjustment was controlled by the use of a pulser, which was set to send calibrated signals at 0.3, 0.45, 0.6, 0.8, 1.3 and 1.6 V, both before and after the adjustment. The positions of the signals were recorded as shown in Figure 2.11. To correct the calibration parameters to the new setup, two linear regressions are made for each detector:

1. Pulser voltage as a function of ADC values after the gain adjustment using the 6 points obtained before ($V = m_a \cdot ADC_a + q_a$).

2. ADC values before the gain adjustment as a function of pulser voltage ($ADC_b = m_b \cdot V + q_b$).

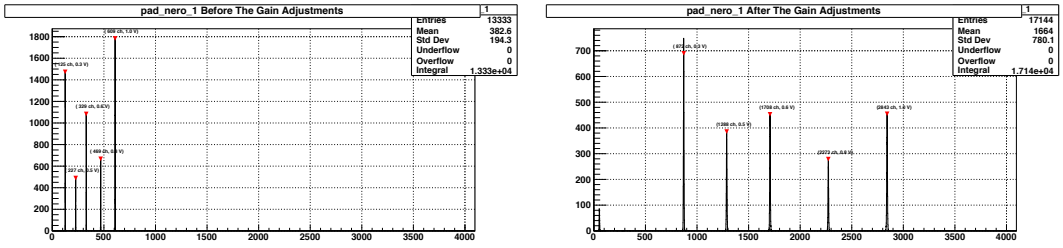

(a) Pad number 1 *OSCAR Nero* before **(b)** Pad number 1 *OSCAR Nero* after

Figure 2.11: Pulser signal positions before and after the gain adjustments.

Given the parameters for the previous calibration from the formula $E = m_1 \cdot ADC_b + q_1$, by writing ADC_b as a function of ADC_1 from the results given from two fits, the parameters are adjusted to provide the new calibration corresponding to the formula $E = m_2 \cdot ADC_a + q_2$.

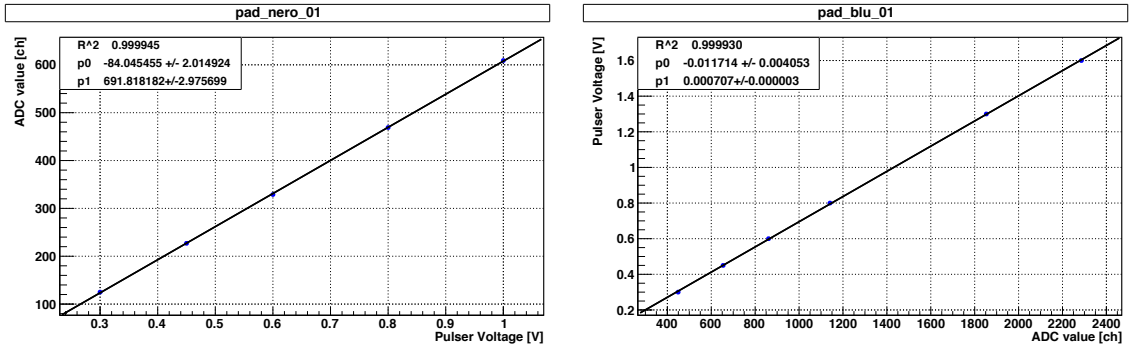

(a) Pad number 1 *OSCAR Nero* before **(b)** Pad number 1 *OSCAR Blu* after

Figure 2.12: Linear regressions

Using the linear fit coefficients, the parameters of *OSCAR Blu* and *Nero*'s pads are corrected to be adapted to the new gain setting. To check the validity of this new set of parameters, the energy spectrum of the two gain adjustment runs for each pad is plotted (in MeV) to see if the peaks align as expected, confirming the good consistency of the procedure.

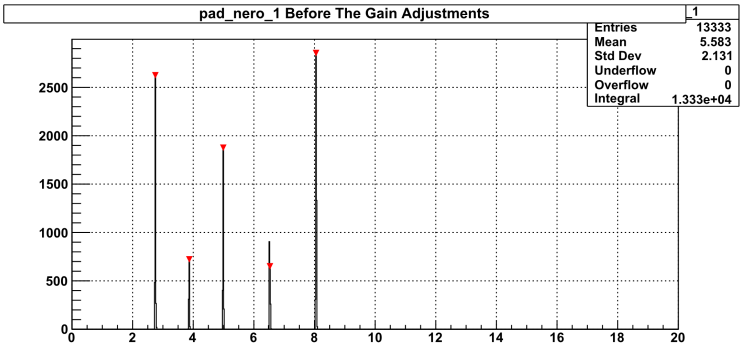

(a) Pad number 1 *OSCAR Nero* before

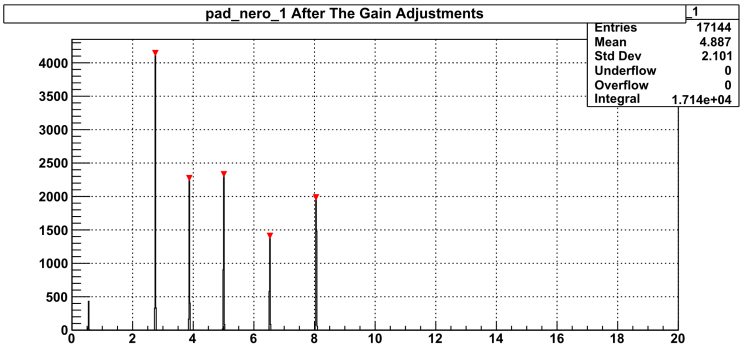

(b) Pad number 1 *OSCAR Nero* after

Figure 2.13: The alignment of pulsar signals

3

Data Analysis and Preliminary Results

3.1 The ΔE-E technique for particle identification

A crucial aspect of experimental nuclear physics is identifying the particles detected in a given event, in other words, determining their mass (A), charge (Z), and kinetic energy (E_k). Among various methods to fulfill this task, such as pulse-shape analysis or trajectory reconstruction, we made use of the ΔE-E technique. ΔE-E telescopes consist of two levels of detection: a first stage (ΔE) is sufficiently thin for the particle to punch through and the second detection stage (E) where the particle is usually fully stopped.

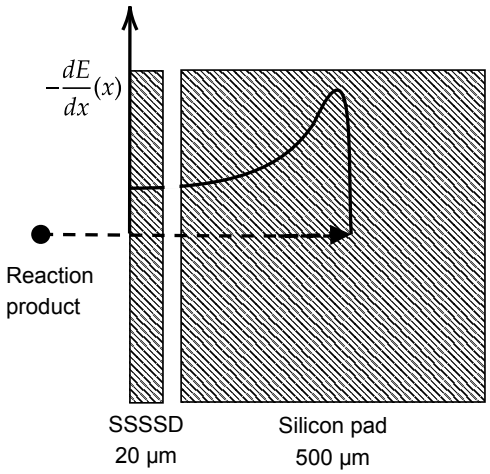

Figure 3.1: Particle energy deposition in a ΔE-E detector of the OSCAR device.

When used to identify heavy charged particles, the first stage slows down and reduces the kinetic energy of the particle according to the stopping power, which gives the energy deposited by the particle in the material per unit length. The stopping power is a function of the nature of the incident particle and that of the material where the particle travels. A possible parametrization is that given by the Bethe-Bloch formula:

$$-\frac{dE}{dx} = \left(\frac{ze^2}{4\pi\epsilon_0}\right)^2 \frac{4\pi Z\rho N_A}{Amv^2}\left[\ln\left(\frac{2mv^2}{I}\right) - \ln(1-\beta^2) - \beta^2\right]$$

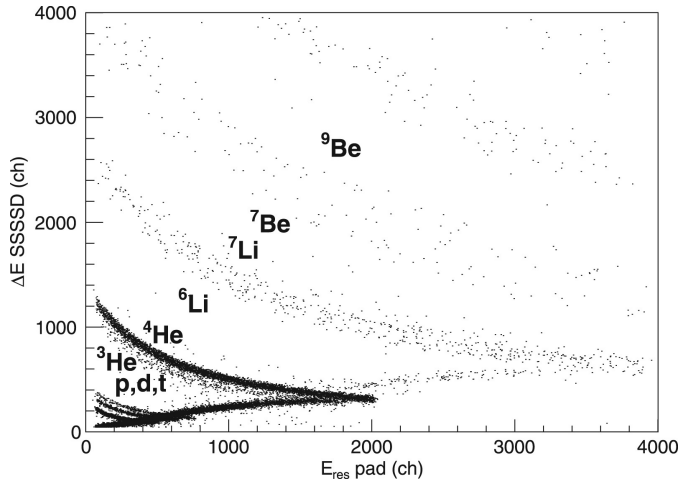

Figure 3.2: Example curves on a ΔE-E plot belonging to different isotopes produced by an OSCAR telescope extracted from Ref. [17].

where Z and A are the charge and mass of the atoms in the material, respectively, I is the mean ionization potential of the atoms in the material, ρ is its density, β is the velocity v of the particle per unit of the speed of light c, z is the charge of the incident particle, m is the mass of an electron, and N_A is the Avogadro number. For a given material and an initial kinetic energy E_k, the partition of energy between two stages depends on the charge and mass of the particle, due to the relation above. This results in the separation of different nuclei to different loci in a ΔE-E histogram, as shown in Figure 3.2.

In the present study, the ΔE-E technique is used to identify detected reaction products and to select the reaction products that are of interest for the investigation, i.e. α-ejectiles from (^{3}He, $\alpha_{0,1,2}$) reactions on ^{13}C. To do so, ΔE-E plots of 8 runs with different energies were initially built, and then graphical cuts that identify alpha particles were performed for each individual detection unit of the apparatus. In this phase of the data reduction, we exploited the previously calibrated energies in both detection stages. The identification of particles is done only for *OSCAR Blu* and *Nero* since they have two detection stages. These two telescopes cover the entire polar angle region. An example application of the identification procedure is shown in Figure 3.3, in which the loci corresponding to α_0, α_1, and α_2 smeared as a result of collecting data from several bombarding energies, are clearly visible. Such a technique can be used to identify all particles that are produced in the collisions. Once the identification is completed for all pseudo-detectors, we can proceed into calculating the cross sections for the reactions of interest.

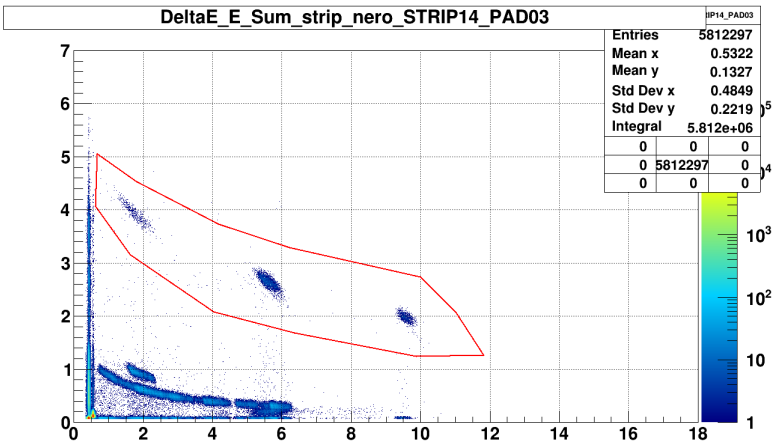

Figure 3.3: Example ΔE-E plot from the present experiment. The region identifying helium-4 of three groups of particles produced during the reaction.

3.2 Absolute cross section

The cross section is a measure of the intrinsic probability with which a nuclear reaction takes place. This is usually referred to as an *effective area* that the target offers to the impinging beam in order for the given reaction to occur. For this reason, it is often measured in barns (10^{-28} m^2), which is a measure of an area. The differential cross section is the cross section per unit solid angle at a given polar angle. The latter is defined as follows:

$$\sigma(\theta) = \frac{d\sigma}{d\Omega}(\theta) = \frac{N_{events}}{N_{inc}\Omega_{det}\mathcal{N}}$$

where N_{inc} is the number of incident particles, Ω_{det} is the solid angle covered by the detector at the polar angle θ, and $\mathcal{N}$ is the number of nuclei per unit surface in the target. N_{events} is deduced experimentally by integrating the area of the peak corresponding to a given nuclear reaction (α_0, α_1, and α_2 in the present case). Since the physical quantity of interest is the cross section in the center-of-mass reference frame, the Ω_{det} should be in this frame of reference. Therefore, the solid angle obtained previously for each unit of detection by the simulation in Ref. [17] is transformed to that of the center of mass by using the *determinant of Jacobian matrix* describing the transformation.

To experimentally determine the number of incident particles, one has to integrate the current measured by the Faraday Cup placed at the end of the beamline, for each experimental run during the whole the duration of the experiment. In addition, due to the unavoidable *deadtime* of the DAQ, not all impinging particles are *effective*. In this experiment, the integrated beam current is corrected by the DAQ *livetime*, i.e. the fraction of the run time in which the DAQ is ready to accept data. This value is estimated using a pulser of calibrated

rate, and by comparing the rate extracted from registered events and the nominal rate of the pulser. Lastly $\mathcal{N}$ is computed from the stoichiometric information regarding the target:

$$\mathcal{N} = \frac{N_{target}}{\Delta S} = n_{target}\Delta x = \frac{\rho dx}{m_{atom}}$$

where n_{target} is the numerical density in cm^{-3}, Δx is the thickness of the target in cm, ρdx is the thickness in $\mathrm{g\,cm}^{-2}$ and m_{atom} is the mass of a single atom in grams. Once the differential cross section is computed for various detection angles, the results are plotted as a function of the angle in center-of-mass reference frame.

In the Quantum Mechanical treatment of nuclear collisions, the incident beam can be considered as a plane wave. The outgoing beam, on the other hand, is the superposition of two components: one that has not interacted with the target, which remains as a plane wave, and one that is deflected, which is represented by a spherical wave with an amplitude $f(\theta)$ depending on the angle and the reaction. The two states of the beam, *ingoing* and *outgoing* are therefore:

$$\Phi_{in} \approx e^{i\boldsymbol{k}\cdot\boldsymbol{r}} \;\; ; \;\; \Phi_{out} \approx e^{i\boldsymbol{k}\cdot\boldsymbol{r}} + f(\theta)\frac{e^{i\boldsymbol{k}\cdot\boldsymbol{r}}}{r}$$

The differential cross section is the ratio between the probability currents of the deflected wave to that of the incident wave, which results to be

$$\frac{d\sigma}{d\Omega}(\theta) = \left|f(\theta)\right|^2$$

It can also be shown that the differential cross section can be written as a series of Legendre polynomials of $\cos(\theta)$ giving the angular dependence. Therefore it is possible to fit angular distributions obtained at various energies with Legendre polynomials in the following way:

$$\frac{d\sigma}{d\Omega}(\theta) = \sum_{l=0}^{l=2l_{max}} B_l P_l(\cos(\theta))$$

where B_l are numerical constants and $P_l(\cos(\theta))$ are the Legendre polynomials, and l_{max} is the maximum order of angular momentum used in the partial-wave decomposition of the cross section. $P_l(x)$ can be written as:

$$P_l(x) = \frac{1}{2^l\, l!}\frac{d^l}{dx^l}(x^2-1)^l$$

In the present study, given the low energies, we consider a maximum value of the orbital angular momentum of the collision of $l_{max} = 2$. Therefore, one can

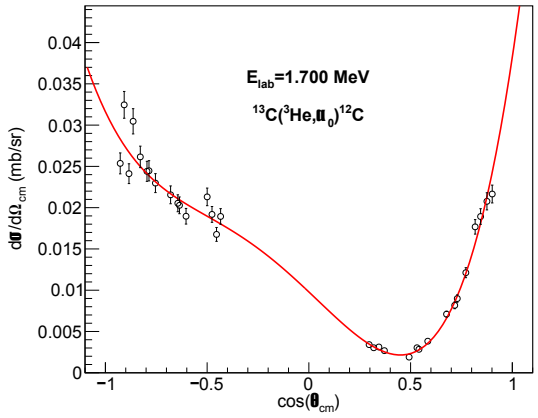

(a) $^{13}C(^{3}He, \alpha_0)^{12}C(g \cdot s)$.

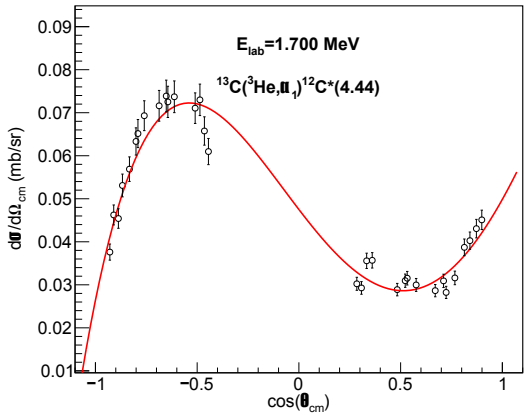

(b) $^{13}C(^{3}He, \alpha_1)^{12}C^*(4.44)$.

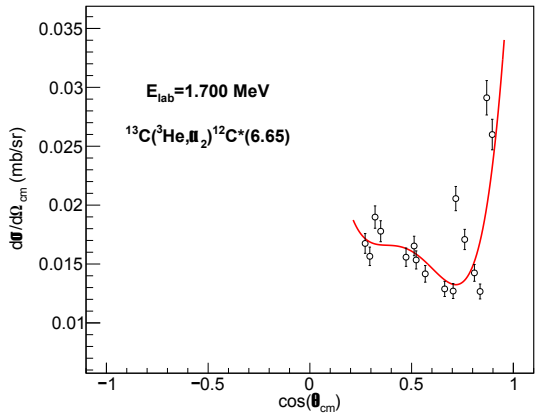

(c) $^{13}C(^{3}He, \alpha_2)^{12}C^*(7.65)$.

Figure 3.4: Angular distributions of $^{13}C(^{3}He, \alpha_{0,1,2})^{12}C$ reactions at $E_{beam} = 1.70$ MeV.

finally obtain:

$$\frac{d\sigma}{d\Omega}(\theta) \approx B_0 + B_1\, P_1(\cos(\theta)) + B_2\, P_2(\cos(\theta)) + B_3\, P_3(\cos(\theta)) + B_4\, P_4(\cos(\theta))$$

The $B_{0\ldots4}$ coefficients are related to the probability of the wave function being described by a given l, and can be extracted from a fit of the experimental data.

For each bombarding energy explored in the present study, we have performed a fit of the corresponding angular distribution obtained by using data from *OSCAR Blu* and *Nero* in the whole angular domain. Some typical angular distributions of the differential cross section of the reactions $^{13}C(^{3}He, \alpha_{0,1,2})^{12}C$, obtained at 1.700 MeV bombarding energy, are shown in Figure 3.4, alongside the corresponding Legendre polynomial fit of data (red line). The experimental errors in the differential cross section values account both for the statistical error associated with the measured counts and integrated beam current and

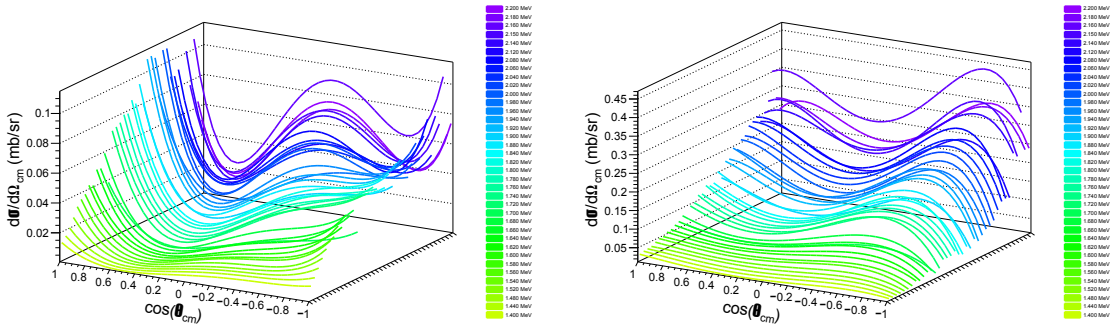

(a) ^{13}C(^{3}He, α_0)^{12}C(g.s). **(b)** ^{13}C(^{3}He, α_1)^{12}C*(4.44).

Figure 3.5: Angular distributions (in CM) of the differential cross section at different bombarding energies.

for the accuracy of the stochiometric information of the target. While for the ^{13}C(^{3}He, $\alpha_{0,1}$)^{12}C reactions we are able to cover the entire relevant angular region, the ^{13}C(^{3}He, α_2)^{12}C reaction is measured only on a limited region of forward angles, as a result of the proximity of ^{4}He ejectiles to the detection threshold. It is clear from Figures 3.4 (a) (b) that the angular distributions of ^{13}C(^{3}He, $\alpha_{0,1}$)^{12}C show asymmetric trends around 90°. For the α_0 case, the angular distribution at 1.700 MeV shows a minimum at 60° and seems to have an increasing trend at forward angles. The shape of the ^{13}C(^{3}He, α_2)^{12}C angular distribution at forward angles is similar to that of ^{13}C(^{3}He, α_0)^{12}C at similar angles, even if the first shows larger absolute values. In fact, both states are 0^+, thus should share a fairly similar angular distribution.

Figure 3.5 shows the result of the Legendre polynomial fits for all bombarding energies investigated in the present experiment for both α_0 and α_1 reactions. Apart from a general increase in the absolute scale of the cross section due to the Coulomb penetrability, the angular distributions show some change in the shape with the energy, which has to be investigated. The α_0 cross section has a minimum at all energies around 60°, while a second local minimum appears at higher energies at backward angles. A sudden change in behavior is seen at 2.180 MeV, which has a higher differential cross section than that lower energy points. This might suggest the occurrence of a resonance in the compound nucleus. Compared to data previously published in the literature, measured angular distributions are in excellent agreement with Ref. [5] at 2 MeV, both in shape and absolute value. It is important to stress that this is so far the only exclusive measurement of the angular distributions of the differential cross section in absolute units for the ^{13}C(^{3}He, $\alpha_{0,1}$)^{12}C reactions in such a broad low energy region.

To meet the purpose of the experiment, we have proceeded into calculating the total absolute cross section by integrating the angular distributions shown above over the entire angular range. This is systematically possible only for

E_{beam}	σ_{α_0} [mb]	σ_{α_1} [mb]	E_{beam}	σ_{α_0} [mb]	σ_{α_1} [mb]
1.400	0.0643 ± 0.0007	0.235 ± 0.003	1.840	0.398 ± 0.005	1.35 ± 0.02
1.440	0.08 ± 0.0008	0.281 ± 0.004	1.880	0.468 ± 0.006	1.58 ± 0.02
1.480	0.095 ± 0.001	0.324 ± 0.004	1.900	0.395 ± 0.005	1.35 ± 0.02
1.520	0.112 ± 0.001	0.374 ± 0.005	1.920	0.499 ± 0.006	1.78 ± 0.02
1.540	0.13 ± 0.001	0.425 ± 0.006	1.940	0.515 ± 0.006	1.83 ± 0.02
1.560	0.155 ± 0.002	0.507 ± 0.007	1.960	0.541 ± 0.007	1.96 ± 0.03
1.580	0.16 ± 0.002	0.532 ± 0.007	1.980	0.477 ± 0.006	1.89 ± 0.03
1.600	0.181 ± 0.002	0.62 ± 0.009	2.000	0.586 ± 0.007	2.1 ± 0.03
1.620	0.189 ± 0.002	0.66 ± 0.009	2.020	0.612 ± 0.008	2.29 ± 0.03
1.640	0.222 ± 0.002	0.76 ± 0.01	2.040	0.576 ± 0.008	2.44 ± 0.03
1.660	0.23 ± 0.002	0.8 ± 0.01	2.060	0.603 ± 0.008	2.6 ± 0.04
1.680	0.272 ± 0.003	0.9 ± 0.01	2.080	0.623 ± 0.008	2.78 ± 0.04
1.700	0.18 ± 0.002	0.6 ± 0.01	2.120	0.53 ± 0.007	2.54 ± 0.04
1.720	0.351 ± 0.004	1.15 ± 0.01	2.140	0.671 ± 0.009	3.23 ± 0.04
1.740	0.354 ± 0.004	1.16 ± 0.02	2.150	0.67 ± 0.01	3.31 ± 0.04
1.760	0.368 ± 0.004	1.24 ± 0.02	2.160	0.86 ± 0.01	4.32 ± 0.06
1.780	0.382 ± 0.004	1.26 ± 0.02	2.180	0.612 ± 0.008	3.2 ± 0.04
1.800	0.401 ± 0.005	1.33 ± 0.02	2.200	0.625 ± 0.009	3.3 ± 0.05
1.820	0.435 ± 0.005	1.41 ± 0.02			

Table 3.1: Integrated cross sections at $1.4 \leq E_{beam} \leq 2.2$MeV.

^{13}C(^{3}He, $\alpha_{0,1}$)^{12}C reactions, where the angular distributions are constrained over the entire angular region. The integrated cross section is thus obtained as

$$\sigma_E = \int_0^{\pi} \int_0^{2\pi} \frac{d\sigma}{d\Omega} d(cos(\theta)) d\phi$$

This results in the integration of the Legendre function $P_n(x)$ between -1 and 1 which is 0 for $n \geq 1$ given the orthogonality relation with $P_0(x)$. Therefore, the total cross section at a given energy simplifies to

$$\sigma(E) = 4\pi b_0$$

The (absolute) total cross section, with its error, is plotted as a function of energy in Figures 3.6a and 3.6b, respectively for α_0 and α_1 reactions. A similar sudden increase is seen at 2.180 MeV, which would correspond to an excitation energy of about 24.56 MeV in the compound ^{16}O nucleus. We are not certain whether or not this peak belongs to a possible resonance structure as it can be a visual effect related to the presence of the local minimum at 2.120 MeV. It is necessary to study further the form of the excitation functions and the variations

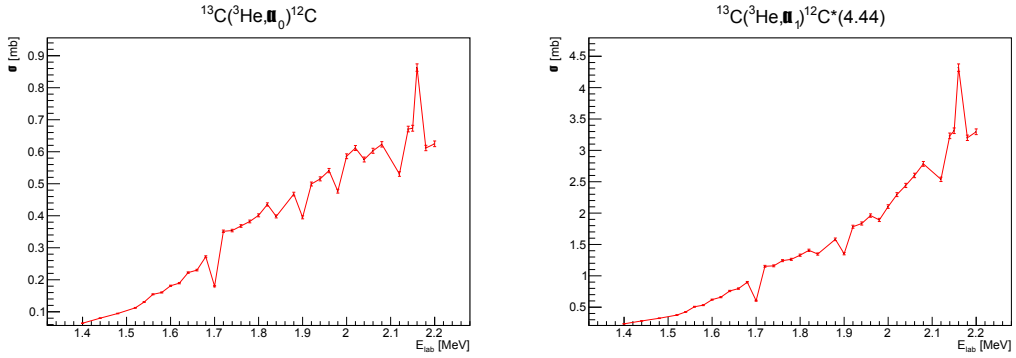

(a) **(b)**

Figure 3.6: Total cross section of $^{13}C(^3He, \alpha_{0,1})^{12}C$ reactions as a function of energy

of the coefficients of the Legendre polynomials (since they identify the angular momentum transferred to the α particle thus the spin and parity of the relevant state of the compound nucleus) to determine the possible correlations with the existing energy levels of the ^{16}O nucleus. This would help to improve the spectroscopy of ^{16}O and to probe the occurrence of direct vs compound nucleus mechanisms in $^{13}C(^3He, \alpha)$ reactions at low energies.

4

Conclusions

In conclusion, this thesis gives an initial outlook into the ^{13}C(^{3}He, $\alpha_{0,1,2}$)^{12}C reactions at sub-Coulomb energies and outlines the experimental procedure used in the HELICA experiment while addressing the main themes regarding the *Experimental Nuclear Physics* at low energies. The work done in the framework of this thesis included a detailed calibration of a complex array of high-resolution silicon detectors. The detection setup used in the present experiment consisted, for the first time, in an arrangement of four OSCAR hodoscopes. The various techniques used in this thesis included common procedures such as the use of a three-peaked α-source along with a clever yet simple use of the ΔE-E plots with the calibrated y-axis to calibrate the second detection stage by making use, also, of experimental data when necessary. The analysis regarding the calibration was carried out swiftly right after the acquisition of the necessary data to provide a basis for the analysis of the actual experimental data.

The thesis provides with the preliminary results of the absolute cross section angular distributions, for the first time in an energy domain ranging from 1.4 to 2.2 MeV, with a large angular range. The angular distributions and the variations of the coefficients of the Legendre polynomials can further be studied to reveal possible correlations between the energy levels of the compound ^{16}O and the occurrence of direct effects. The presently measured angular distributions have been exploited to produce the energy dependence of the absolute integrated cross section for the ^{13}C(^{3}He, $\alpha_{0,1}$)^{12}C reactions. Other reaction channels, such as ^{15}N + p, ^{14}N + d or the elastic scattering of He-3 particles (through the elastic monitor detection unit assigned to this purpose), can be studied in the present experiment to provide with a more complete picture of the consequences of ^{3}He + ^{13}C collision and deeper understanding of the energy region concerned of the compound nucleus.

The work presented in this thesis brings out key points for future studies regarding low-energy nuclear reactions with high-resolution apparatus and presents a great opportunity to deepen knowledge in *Experimental Nuclear Physics* with light ions.

References

[1] E. M. Kellogg and R. W. Zurmühle. "$C^{13}(He^3, \alpha)C^{12}$ Reaction and Elastic Scattering of He^3 from C^{13} at 12, 15, and 18 MeV". In: *Phys. Rev.* 152 (3 Dec. 1966), pp. 890–899.

[2] V.K. Deshpande. "The (He3,) reaction on C13". In: *Nuclear Physics* 70.3 (1965), pp. 561–566.

[3] I. Gulamov et al. "Comparative analysis of (p, d), (d, t) and (3He,) reactions on13C nucleus". In: *Czechoslovak Journal of Physics* 40 (Aug. 1990), pp. 875–894.

[4] Maulen Nassurlla et al. "Study of the 13C(3He,)12C reaction at energies of 50 and 60 MeV". In: *Physica Scripta* 97.4 (Mar. 2022), p. 045302.

[5] H. D. Holmgren. "Differential Cross Section for the $C^{13}(He^3, \alpha)C^{12}$ Reaction at 2.00 Mev". In: *Phys. Rev.* 106 (1 Apr. 1957), pp. 100–101.

[6] H. D. Holmgren et al. "$C^{13}(He^3, \alpha)C^{12}$ Angular Distributions at 4.5 Mev". In: *Phys. Rev.* 106 (1 Apr. 1957), pp. 102–104.

[7] H.R. Weller, N.R. Roberson, and D.R. Tilley. "A study of some 3He induced reactions on 13C and the structure of 16O". In: *Nuclear Physics A* 122.3 (1968), pp. 529–556.

[8] M. A. Eswaran, Suresh Kumar, and E. T. Mirgule. "Direct cluster transfer in ^{3}He bombardment of ^{13}C at sub-barrier energies". In: *Phys. Rev. C* 42 (3 Sept. 1990), pp. 1036–1042.

[9] P. K. Swart et al. "Interstellar Carbon in Meteorites". In: *Science* 220.4595 (1983), pp. 406–410.

[10] Thomas Piper and Mario Thevis. "Investigations in carbon isotope ratios of seized testosterone and boldenone preparations". In: *Drug Testing and Analysis* 14.3 (2022), pp. 514–518.

[11] Illa Tea et al. "13C and 15N natural isotope abundance reflects breast cancer cell metabolism". In: *Scientific Reports* 6 (Sept. 2016).

[12] W.J. Huang et al. "The AME 2020 atomic mass evaluation (I). Evaluation of input data, and adjustment procedures*". In: *Chinese Physics C* 45.3 (Mar. 2021), p. 030002.

[13] Meng Wang et al. “The AME 2020 atomic mass evaluation (II). Tables, graphs and references*”. In: *Chinese Physics C* 45.3 (Mar. 2021), p. 030003.

[14] *National Nuclear Data Center*. URL: https://www.nndc.bnl.gov/.

[15] TUNL Nuclear Data Evaluation Project. *Energy Level Diagram, 16O (1993)*. URL: https://nucldata.tunl.duke.edu/nucldata/figures/16figs/16_08_1993.pdf. (accessed: 12.11.2022).

[16] Akito Arima, Vincent Gillet, and Joseph Ginocchio. “Energies of Quartet Structures in Even-Even $N = Z$ Nuclei”. In: *Phys. Rev. Lett.* 25 (15 Oct. 1970), pp. 1043–1046.

[17] Daniele Dell’Aquila et al. “OSCAR: A new modular device for the identification and correlation of low energy particles”. In: *Nuclear Instruments and Methods in Physics Research Section A: Accelerators, Spectrometers, Detectors and Associated Equipment* 877 (Oct. 2017).

[18] Nóra Vajda et al. “Chapter 5 - Alpha spectrometry”. In: *Handbook of Radioactivity Analysis (Fourth Edition)*. Ed. by Michael F. L’Annunziata. Fourth Edition. Academic Press, 2020, pp. 493–573.

[19] O.B. Tarasov and D. Bazin. “LISE++: Radioactive beam production with in-flight separators”. In: *Nuclear Instruments and Methods in Physics Research Section B: Beam Interactions with Materials and Atoms* 266.19 (2008). Proceedings of the XVth International Conference on Electromagnetic Isotope Separators and Techniques Related to their Applications, pp. 4657–4664.